DOI 10.1007/s12182-014-0326-5

Properties of oxide films grown on 25Cr20Ni alloy in air-H_2O and H_2-H_2O atmospheres

Wang Shenxiang[1, 2], Cui Lishan[1]*, Wang Guoqing[2], Zheng Yanjun[1], Wang Hongxia[2] and Jia Jingsheng[2]

[1] College of Science, China University of Petroleum, Beijing 102249, China
[2] Beijing Research Institute of Chemical Industry, Beijing 100013, China

Abstract: The oxidation kinetics, surface morphology and phase structure of oxide films grown on 25Cr20Ni alloy in air-H_2O and H_2-H_2O atmospheres at 900 °C for 20 h were investigated. The anti-coking performance and resistance to carburization of the two oxide films were compared using 25Cr20Ni alloy tubes with an inner diameter of 10 mm and a length of 850 mm in a bench scale naphtha steam pyrolysis unit. The oxidation kinetics followed a parabolic law in an air-H_2O atmosphere and a logarithm law in a H_2-H_2O atmosphere in the steady-state stage. The oxide film grown in the air-H_2O atmosphere had cracks where the elements Fe and Ni were enriched and the un-cracked area was covered with octahedral-shaped $MnCr_2O_4$ spinels and $Cr_{1.3}Fe_{0.7}O_3$ oxide clusters, while the oxide film grown in the H_2-H_2O atmosphere was intact and completely covered with dense standing blade $MnCr_2O_4$ spinels. In the pyrolysis tests, the anti-coking performance and resistance to carburization of the oxide film grown in the H_2-H_2O atmosphere were far better than that in the air-H_2O atmosphere. The mass of coke formed in the oxide film grown in the H_2-H_2O atmosphere was less than 10% of that in the air-H_2O atmosphere. The $Cr_{1.3}Fe_{0.7}O_3$ oxide clusters converted into $Cr_{23}C_6$ carbides and the cracks were filled with carbon in the oxide film grown in the air-H_2O atmosphere after repeated coking and decoking tests, while the dense standing blade $MnCr_2O_4$ spinels remained unchanged in the oxide film grown in the H_2-H_2O atmosphere. The ethylene, propylene and butadiene yields in the pyrolysis tests were almost the same for the two oxide films.

Key words: 25Cr20Ni alloy, air-H_2O, H_2-H_2O, oxide film, anti-coking, resistance to carburization

1 Introduction

Ethylene is one of the most important basic materials in the petrochemical industry, and steam pyrolysis of hydrocarbons is the major process for producing ethylene nowadays. Coke always deposits on the internal surface of the radiant coils of the pyrolysis furnace in hydrocarbon pyrolysis. Coke is a poor conductor of heat and it decreases the heat transmission of the radiant coil, resulting in a temperature increase in the outside surface of the radiant coil. When the temperature of the outside surface reaches the maximum temperate limit of the alloy material, the radiant coils have to be decoked. So coke deposition on the internal surface of the radiant coil is the main factor that affects the production cycle of the pyrolysis furnace.

The alloy of the radiant coil is mainly made of elements Fe, Cr, and Ni. The elements, Fe and Ni, have a strong catalytic effect on the coke formation at high temperatures, so the inner surface is always covered with filamentous catalytic coke in the early service of the radiant coil (Baker, 1989; Bonnet et al, 2003). The tar drops in the pyrolysis gas can be easily adsorbed onto the surface of the filamentous coke (Cai, 2002), then they turn into dense coke adhered to the inner surface after further dehydrogenation (Albright and Marek, 1988; Manafzadeh et al, 2003). Meanwhile, free radicals (such as methyl, ethyl etc) on the filamentous coke can react with small hydrocarbon molecules (such as ethyne, ethylene etc) to form polyaromatic hydrocarbons (Towfighi et al, 2002). After further condensation and dehydrogenation, polyaromatic hydrocarbons form into new coke which expands the diameter of the filamentous coke (Deng et al, 2000). Consequently, the formation of catalytic coke is the base of coke deposition on the inner surface in hydrocarbon pyrolysis, and reducing the contents of elements Fe and Ni on the inner surface of the radiant coil is the key factor of coking inhibition.

Since the 1980s, many investigators have explored the coating technologies to reduce the contents of elements Fe and Ni on the inner surface of the radiant coil (Wynns and Bayer, 2003; Fisher et al, 2003; Zhou et al, 2012), but these coatings could not be used in the industrial process due to their short service life. In fact, the pre-oxidation technology

*Corresponding author. email: lishancui63@126.com
Received March 21, 2013

of the inner surface has been widely used for coking inhibition in new radiant coils which are pre-oxidized using an air-H_2O mixture before they are put into service. Nova Chemicals Corporation (Benum and Oballa, 2002; Benum et al, 2004; 2009) invented a better pre-oxidation technology which could prolong the production cycle of pyrolysis furnaces dramatically. The new pre-oxidation technologies are performed under low oxygen partial pressure in a H_2-H_2O atmosphere. The two pre-oxidation technologies have been used in the industrial process, but the mechanisms of coking inhibition and resistance to carburization have not been further studied. In this investigation, the 25Cr20Ni alloy is used as the material and its oxidation kinetics, surface morphology and phase structure oxidized in air-H_2O and H_2-H_2O atmospheres are investigated. The anti-coking performance and resistance to carburization are compared in 25Cr20Ni mini tubes pre-oxidized in the two different atmospheres.

2 Experimental material and methods

2.1 Preparation and oxidation of samples

The material used in this investigation was 25Cr20Ni alloy, and its nominal chemical composition is listed in Table 1. Samples, with a dimension of 20mm×10mm×2mm, were machined by a computerized numerical control (CNC) wire-cut machine. The surface roughness was about 1.6 μm. The samples were cleaned with acetone and deionized water in an ultrasonic cleaner before oxidation.

Table 1 Composition of the 25Cr20Ni alloy

Element	C	Si	Mn	P	S	Cr	Ni	Fe
Content, wt%	0.046	0.48	0.63	0.029	0.013	24.39	19.20	Balance

The isothermal oxidation tests of the samples were performed in a thermo-gravimetric analyzer (Cahn Versa Therm HM) at 900 ºC in an oxidizing gas for 20 h. Air-H_2O or H_2-H_2O mixtures were used as the oxidizing gas with a flow rate of 100 mL/min. The heating rate of the thermo-gravimetric analyzer was 10 ºC/min, and the cooling rate was 2 ºC/min. When the oxidizing gas was the H_2-H_2O mixture, the air was exhausted from the reactor by a vacuum pump at room temperature before the test. The air-H_2O or H_2-H_2O mixture was obtained by bubbling air or high purity H_2 through a deionized water flask. The deionized water temperature was controlled at 20 ºC by a thermostatic water cabinet.

2.2 Preparation and oxidation of mini tube

The material of the mini tube was 25Cr20Ni alloy, which was consistent with the samples above. The mini tube had an inside diameter of 10 mm and a length of 850 mm. The inner surfaces of the tubes were treated by a reamer to remove the oxide-scale and to reduce the surface roughness to about 1.6 μm. The tubes were then cleaned with acetone and deionized water before oxidation.

The isothermal oxidation tests of the tubes were performed in a bench scale pyrolysis unit (Fig. 1) at 900 ºC in the oxidizing gas for 20 h. Air-H_2O or H_2-H_2O mixture was led into the tube from the cross section at a flow rate of 300 mL/min. The heating rate of tube was 20 ºC/min, and the tube cooled naturally in the furnace after the oxidation test.

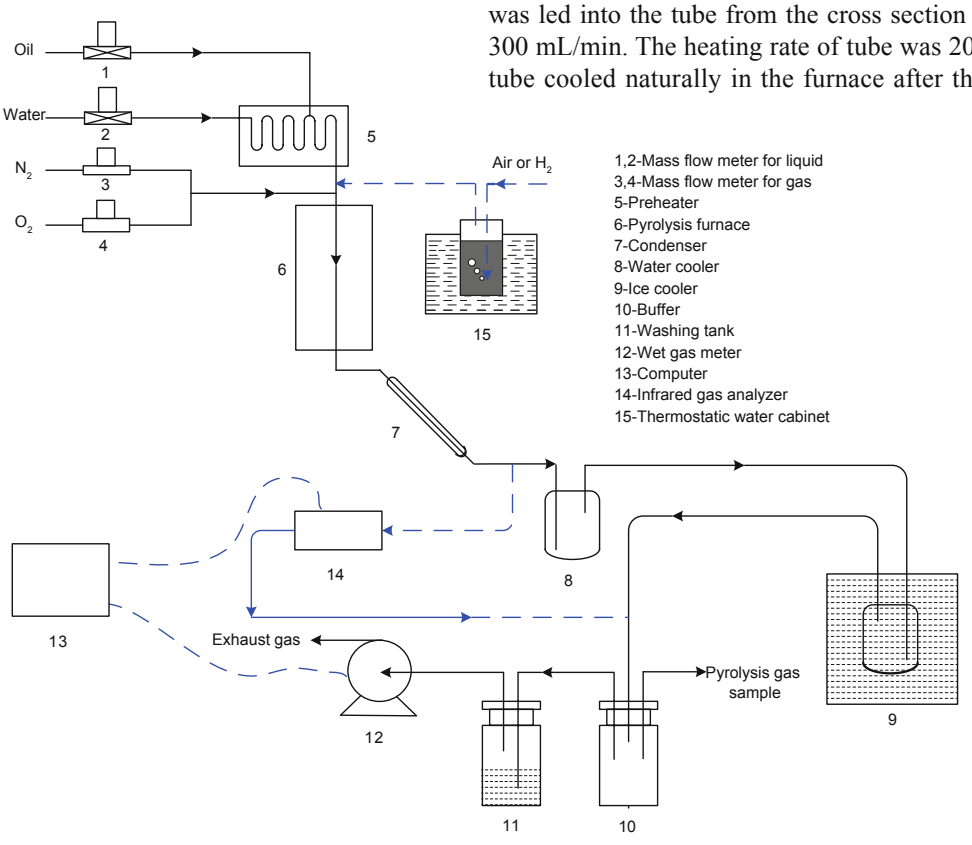

Fig. 1 Bench scale pyrolysis and coking test unit

When the oxidizing gas was the H_2-H_2O mixture, the air was exhausted from the pyrolysis unit by a vacuum pump at room temperature before the test.

2.3 Pyrolysis and coking test of the mini tubes

The pyrolysis feedstock in this test was naphtha and its physical properties and group composition are listed in Table 2. The mini tube pyrolysis and coking test was performed in a bench scale pyrolysis unit (Fig. 1).

The preheater and pyrolysis furnace tube were heated up at the heating rate of 10 and 20 ºC/min, until their temperatures reached 600 and 850 ºC, respectively. Water was injected into the preheater at a flow rate of 50 g/h during the temperature-rise period. During the constant temperature phase, naphtha was let into the preheater at a flow rate of 100 g/h, and the water flow rate was still 50 g/h. The naphtha and water were gasified and mixed in the preheater, then flowed into the pyrolysis furnace tube to be pyrolyzed. The pyrolysis products from the high temperature tube passed though the condenser, water cooler, ice cooler, buffer, washing tank, wet gas meter, and were emitted. The pyrolysis gas sample was taken from the buffer bottle, and its compositions and concentrations were analyzed by gas chromatography (AGILENT TECHNOLOGIES 6890N). The yields of the pyrolysis products could be calculated according to the parameters, such as volume, compositions, and concentrations of pyrolysis gas, mass and properties of feedstock, etc.

After the pyrolysis had lasted for 2 h, the water and naphtha flows were stopped. The temperature of the pyrolysis furnace tube cooled to 820 ºC, then the tube was purged with nitrogen at a flow rate of 1 L/min. After purging the tube for about15 min, oxygen was let into the tube at a flow rate between 0.1 L/min and 0.3 L/min to burn the coke deposited on the internal surface of the tube, meanwhile the nitrogen flow rate was remained unchanged. The concentrations of CO and CO_2 in the decoking off-gas were monitored on line by an infrared gas analyzer (SIEMENS ULTRAMAT 23). The volume of off-gas was measured by the wet gas meter. The concentration and volume data were transferred into the computer, and the mass of the coke which deposited on the internal surface of the tube could be calculated.

Table 2 Properties and group composition of naphtha

Properties		Group composition, wt%	
Density d_4^{20}	0.74	Alkane	30.62
Average molecular mass	112.37	Isoalkane	32.18
API gravity	59.00	Olefin	0.13
Bureau of Mines Correlation Index (BMCI)	18.22	Naphthene	31.13
Characterization factor K^{uop}	12.00	Aromatics	5.73
Refractive index n_D^{20}	1.42	Unknown	0.21

2.4 Analysis and characterization

The surface morphology and microstructure of the oxide films on the samples were characterized with a scanning electron microscope (FEI XL-30) with an acceleration voltage of 15 kV. The element contents of the oxide film were analyzed with an energy dispersive X-ray spectrometer (EDAX Apollo XP). The phases of the oxide film were determined with an X-ray diffractometer (Bruker D8 ADVANCE). The scanning range 2θ was from 5° to 80º and the scanning rate was 8 °/min. Cu Kα incident radiation generated at 40 kV and 30 mA was used for diffraction.

3 Results and discussion

3.1 Oxidation kinetics

The two mass gain curves during isothermal oxidation of the 25Cr20Ni samples in air-H_2O and H_2-H_2O atmospheres at 900 ºC for 20 h were shown in Fig. 2. Each mass gain curve could be schematically divided into two stages, the initial oxidation stage and the steady-state oxidation stage. The two mass gain curves were fitted into four curves *a*, *b*, *c*, *d* in Fig. 2 with Origin Soft. Their fitting equations were y=0.57397x+0.00403, y^2=0.27626x−0.07502, y=0.435x+0.03, y=0.36816ln(x+1.12048)+0.24574. So the oxidation kinetics in the air-H_2O atmosphere followed a linear law in the initial stage of 0-0.6 h (Curve *a*) and a parabolic law in the steady-state stage of 0.6-20 h (Curve *b*). The oxidation kinetics in the H_2-H_2O atmosphere followed a linear law in the initial stage of 0-1.1 h (Curve *c*) and a logarithm law in the steady-state

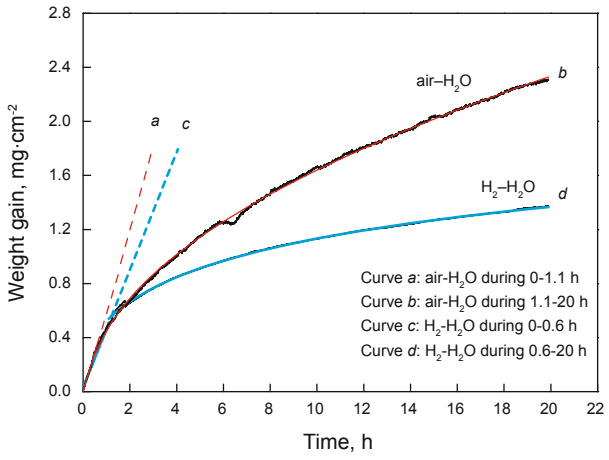

Fig. 2 Mass gains and fitting curves of samples in different atmospheres at different oxidation stages

stage of 1.1-20 h (Curve *d*).

When the oxidation kinetics followed the linear law, the growth rate of the oxide film was controlled by the reaction of metal with oxygen (Li, 2003). So the oxidation rate in air-H_2O was faster than that in H_2-H_2O due to its higher oxygen concentration, so the slope of line *a* was higher than line *c*. When the oxidation kinetics in air-H_2O followed the parabolic law, the growth rate depended on the ion diffusion rate, which was controlled by the concentration gradient of metal and oxygen ions which was inversely proportional to the thickness of oxide film (Li,

2003). This was the reason that the growth rate tended to slow down with the increment in thickness of oxide film, as shown as curve *b* in Fig. 2. When the oxidation kinetics in H_2-H_2O followed the logarithm law, the ion diffusion rate was controlled by the electric potential gradient in the oxide film generated by the electrons that moved outward from the interface to the external surface (Pan and Li, 1959). The electric potential gradient decreased exponentially with the increment in the thickness (Mott and Curney, 1940), so it was more and more difficult for the ions to diffuse and the oxidation rate decreased dramatically, as shown as curve *d* in Fig. 2. The pressure stress in the oxide film grown in H_2-H_2O was also in gradient distribution, and the pressure stress was highest on the external surface (Kofstad, 1988), so the vacancy defects in the oxide film moved inward, resulting in the external surface of the oxide film becoming very dense. This was the reason that the oxide film grown in H_2-H_2O was more protective for the matrix alloy.

3.2 Surface morphology and phase structure of oxide films

The surface morphologies of the oxide films grown in air-H_2O and H_2-H_2O atmospheres at 900 ºC for 20 h were shown in Fig. 3. The element contents in different positions in Fig. 3 were analyzed by EDS, as listed in Table 3. The XRD patterns of the two oxide films are shown in Fig. 4 and the peaks of Fe-Ni phase were from the matrix alloy.

It was found that the oxide film grown in air-H_2O had cracks (Fig. 3(a), Fig. 3(b)), where the elements Fe and Ni were enriched (point 1 in Fig. 3(b)) and the un-cracked

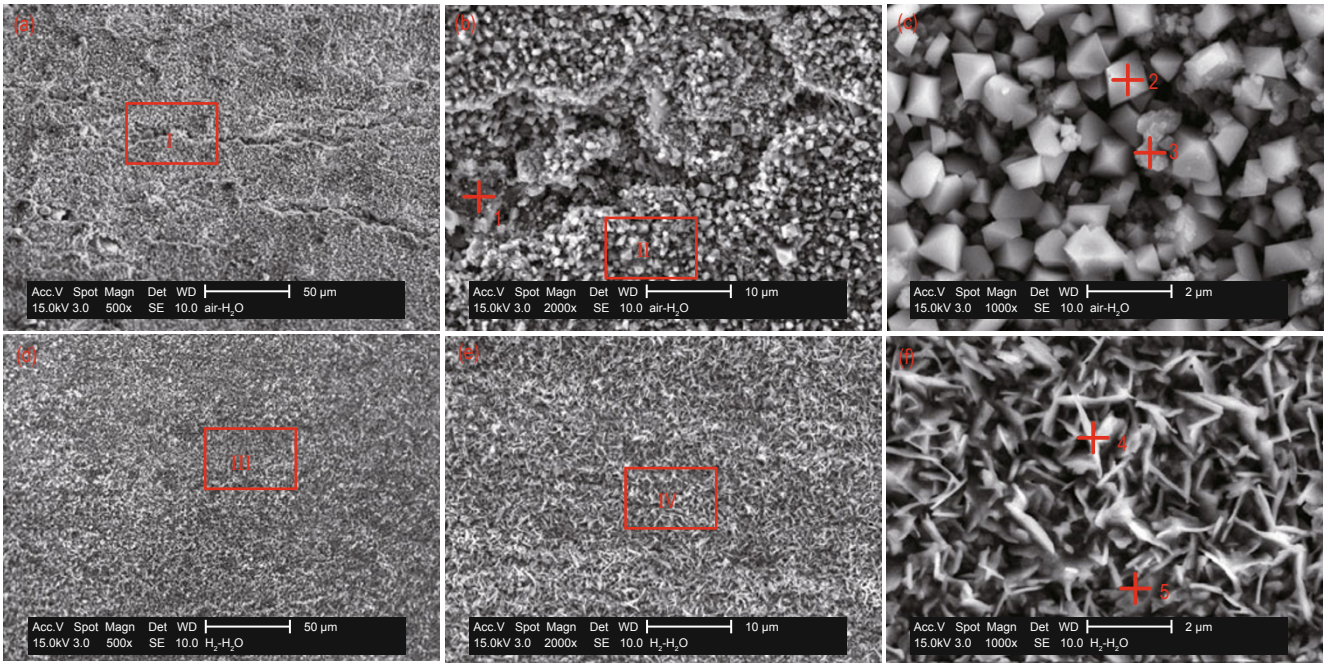

Fig. 3 Surface morphology of the oxide films oxidized in different atmospheres
(a) Air-H_2O; (b) Magnification of area I; (c) Magnification of area II;
(d) H_2-H_2O; (e) Magnification of area III; (f) Magnification of area IV

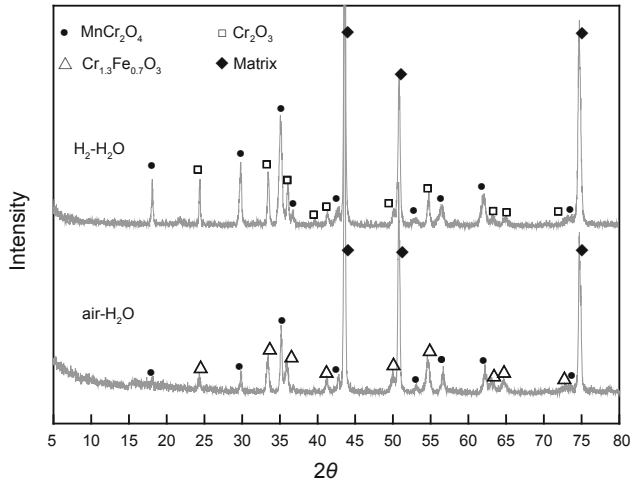

Fig. 4 XRD patterns of the oxide films oxidized in different atmospheres

area was covered with octahedral-shaped crystallites (point 2 in Fig. 3(c)) and clusters of grains (point 3 in Fig. 3(c)), while the oxide film grown in H_2-H_2O was intact (Fig. 3(d), Fig. 3(e)) and completely covered with dense standing blades (point 4, point 5 in Fig.3(f)). According to the XRD analysis results, the oxide film grown in air-H_2O consisted of $MnCr_2O_4$ spinels and $Cr_{1.3}Fe_{0.7}O_3$ oxides, and the oxide film grown in H_2-H_2O consisted of $MnCr_2O_4$ spinels and Cr_2O_3 oxides. Combining this with the EDS analysis results, it was concluded that both the octahedral-shaped crystallites and the standing blades were $MnCr_2O_4$ spinels, and the clusters of grains were $Cr_{1.3}Fe_{0.7}O_3$ oxides. The standing blade $MnCr_2O_4$ spinels on the oxide film grown in H_2-H_2O were so dense that Cr_2O_3 oxides under the $MnCr_2O_4$ spinels (Susan et al, 2009) were barely observed by SEM. However, there were many gaps between the octahedral-shaped $MnCr_2O_4$ spinels

on the oxide film grown in air-H_2O which were filled with $Cr_{1.3}Fe_{0.7}O_3$ oxides.

The cracks could be explained from the way of releasing the growth stresses. When the new oxides (such as Cr_2O_3, Fe_2O_3, MnO) were generated continuously, the growth stresses were accumulated inside the oxide film. The grain size of the oxide film grown in air-H_2O was larger than that in H_2-H_2O, and the growth stresses in the oxide film grown in air-H_2O were released by the way of cracking rather than the way of deformation of creep in the oxide film grown in H_2-H_2O (Zurek et al, 2008). On the other hand, the cracks were related to the thickness of the oxide film. The mass gains of the two oxide films were 2.30 and 1.37 mg/cm^2, and the density of the oxides (such as Cr_2O_3, Fe_2O_3, MnO) was about 5.2 g/cm^3, so the thicknesses of the two oxide films were 4.4 and 2.6 μm, respectively. The thicker the oxide film was, the bigger was the thermal expansivity difference between matrix alloy and oxide film. So the oxide film grown in air-H_2O was easier to crack during pyrolysis. The total content of elements Fe and Ni was close to 70% (point 1 in Table 3) in the cracks. The formation of catalytic coke would inevitably occur in these areas in the pyrolysis environment.

Table 3 Contents of elements in different positions in Fig. 3 (wt%)

Element	Point 1	Point 2	Point 3	Point 4	Point 5	Area II	Area IV
O	17.19	53.23	53.57	51.35	54.41	51.10	54.95
Si	4.20	0.31	0.98	0.66	0.60	0.88	0.59
Cr	8.58	29.85	28.47	30.48	29.23	29.88	29.18
Mn	1.47	14.22	1.52	14.90	13.53	6.23	13.70
Fe	38.90	1.86	13.45	2.01	1.78	10.84	1.14
Ni	29.66	0.53	2.01	0.60	0.45	1.07	0.45

The oxide formation on the surface of 25Cr20Ni alloy could be explained by the affinity of the elements Fe, Ni, Cr and Mn for oxygen. Through calculation on oxygen partial pressures required to form oxides of the four metals at 900 °C using data provided by Povoden et al (2006), it could be determined that the order of affinity for oxygen was: Mn > Cr > Fe > Ni, as listed in Table 4. The oxygen partial pressure of H_2-H_2O mixture at 900 °C whose dew point was 20 °C was 3.42×10^{-20} atm calculated with Eq. (1) (Hua et al, 2009). So Mn and Cr were oxidized into MnO and Cr_2O_3 and Fe, Ni were not oxidized in the H_2-H_2O atmosphere. This was the reason that the oxide film grown in H_2-H_2O contained a large amount of Cr, Mn and a very small amount of Fe, Ni. The oxygen partial pressure of the air-H_2O mixture was about 0.21 atm which was far above that required to form the corresponding oxides, and Mn, Cr, Fe and Ni were all oxidized, into MnO, Cr_2O_3, Fe_2O_3, NiO respectively. So there were more Fe, Ni in the oxide film grown in air-H_2O than that in H_2-H_2O.

$$\frac{P_{O_2}}{P^{\theta}}=\left[\frac{P_{H_2O}}{P_{H_2}}\right]^2\left[\exp\frac{-246000+54.8T}{8.314T}\right]^2 \quad (1)$$

Table 4 Oxygen partial pressures required to form oxides of various metals at 900 °C

Oxide	Oxygen partial pressures, atm
MnO	2.02×10^{-27}
Cr_2O_3	6.23×10^{-25}
Fe_2O_3	1.25×10^{-15}
NiO	3.29×10^{-12}

The high content of Mn on the oxide film surface could be explained from the diffusivity. The outward diffusivity of Cr, Fe and Ni through the initially formed oxide film was within the same order of magnitude (Lobnig, 1992), but Mn diffused at a rate about two orders of magnitude greater than Cr (Lobnig, 1992). So even though the content of Mn was less than 1% in the matrix alloy, it could still diffuse to the oxide film external surface.

The morphology difference of $MnCr_2O_4$ spinels formed in air-H_2O and H_2-H_2O atmospheres could be explained from their growth mechanisms. Raynaud and Rapp (1984) thought the standing blade spinels $MnCr_2O_4$ grew mainly along the grain boundaries in the H_2-H_2O atmosphere. The Mn and Cr ions preferred to diffuse outward along the oxide grain boundaries rather than in the grains, so there were large amounts of MnO and Cr_2O_3 oxides along the grain boundaries which formed the protuberances with fast diffusion paths. In the H_2-H_2O atmosphere, the oxidizing medium was H_2O, which could be catalytically decomposed into oxygen atoms by the protuberances (Polman, 1989), and lots of oxygen atoms were absorbed on the protuberances, resulting in the protuberances growing larger and larger. Finally the protuberances evolved into the standing blade oxides along the grain boundaries (Raynaud and Rapp, 1984). On the top of the standing blade oxides, MnO reacted with Cr_2O_3 to form $MnCr_2O_4$ spinels, which were usually above the excess Cr_2O_3 and a double-layer oxide film $MnCr_2O_4$/Cr_2O_3 formed (Hammer et al, 2007; Susan et al, 2009). In the air-H_2O atmosphere, the oxidizing medium was O_2 instead of H_2O (Hänsel et al, 2003). The oxygen atoms decomposed from O_2 could be absorbed not only on the protuberances along the gain boundaries but on the whole surface, so the appearance of $MnCr_2O_4$ spinel was not the standing blade but the usual octahedral-shaped crystallites. In the air-H_2O atmosphere, the excess Cr_2O_3 reacted with Fe_2O_3 to form $Cr_{1.3}Fe_{0.7}O_3$.

3.3 Coking test of oxide film

Fig. 5 shows the mass of coke during 10 short pyrolysis cycles of the mini tubes oxidized in air-H_2O and H_2-H_2O atmospheres at 900 °C for 20 h. It was found that the mass of coke formed in the tube oxidized in air-H_2O increased gradually in the first five cycles and the mass of coke stayed at about 1.2 g in the later five cycles. The mass of coke formed in the tube oxidized in H_2-H_2O stayed at about 0.1 g in the ten cycles. So the anti-coking performance of the tube oxidized in H_2-H_2O was far better than that in air-H_2O. The mass of coke formed in the tube oxidized in H_2-H_2O was only

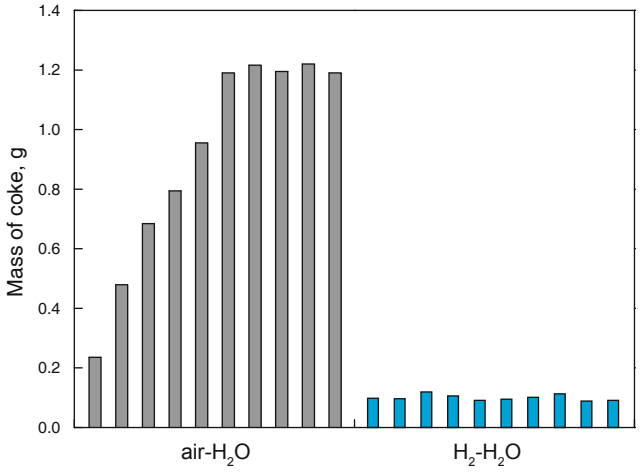

Fig. 5 Mass of coke in mini tubes oxidized in different atmospheres

8% of that in air-H_2O when the mass of coke stabilized after repeated coking and decoking tests.

The inner surface morphologies of the mini tubes after the 10 coking and decoking tests are shown in Fig. 6. The element contents in different positions in Fig. 6 were analyzed with the EDS, as listed in Table 5. The XRD patterns of the two inner surfaces are shown in Fig. 7 and the peaks of Fe-Ni phase were from the matrix alloy.

It was found that there were many cracks (Fig. 6(a), Fig.6(b)) on the inner surface oxidized in air-H_2O after repeated coking and decoking tests, while the inner surface oxidized in H_2-H_2O was still covered with dense standing blades of $MnCr_2O_4$ spinels (point 5, point 6 in Fig. 6(f)). From the EDS and XRD results, it was inferred that the inner surface oxidized in air-H_2O was carbonized (Fig. 6(b), Fig. 6(c)) except the octahedral-shaped $MnCr_2O_4$ spinels (point 2 in Fig. 6(c)). The $Cr_{1.3}Fe_{0.7}O_3$ oxide clusters converted into $Cr_{23}C_6$ carbides (point 3, point 4 in Fig. 6(c)), and the carbon agglomerates were detected in the cracks (point 1 in Fig. 6(b)).

Table 5 Contents of elements in different positions in Fig. 6 (wt%)

Element	Point 1	Point 2	Point 3	Point 4	Point 5	Point 6	Area II	Area IV
C	54.80	0.34	16.05	10.87	0.37	0.57	13.35	0.75
O	24.24	55.54	19.16	21.51	50.73	53.72	39.54	50.24
Si	0.41	0.83	0.45	1.29	1.41	2.29	0.83	1.66
Cr	7.77	27.18	51.08	43.76	30.91	28.58	23.67	31.41
Mn	2.53	14.06	0.25	3.53	14.63	12.21	10.37	12.63
Fe	5.85	1.16	12.60	18.63	1.21	2.17	11.74	1.97
Ni	4.40	0.89	0.41	0.41	0.74	0.46	0.50	1.34

In the pyrolysis test, a large number of hydrocarbon radicals adsorbed on the inner surface and decomposed into carbon on the high energy surfaces of Fe, Ni catalytic particles, and then the carbon precipitated on the low energy surfaces (Baker et al, 1975; Baker, 1989; Li et al, 2001). This process repeated continuously, resulting in the precipitated carbon growing into the filamentous coke, which filled in the cracks (point 1 in Fig. 6(b)) on the inner surface oxidized in air-H_2O where Fe and Ni were enriched. There were more and more cracks on the inner surface after repeated coking and decoking tests, which would seriously weaken its anti-coking performance. On the other hand, the $Cr_{1.3}Fe_{0.7}O_3$ oxide clusters in the un-cracked areas converted into large-grained $Cr_{23}C_6$ carbides (point 3 in Fig. 6(c)). These were the main reasons that the mass of coke of the tube oxidized in air-H_2O increased gradually in the first five cycles. However,

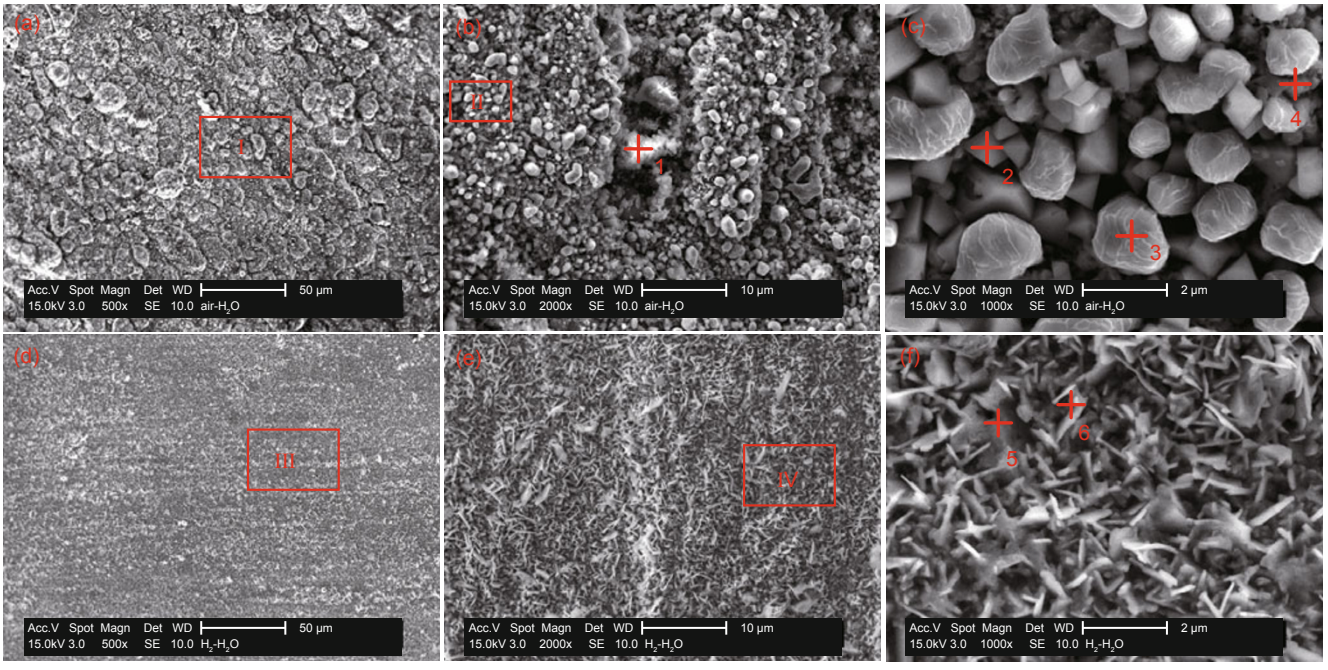

Fig. 6 Inner surface morphology of mini tubes after 10 coking and decoking tests
(a) Air-H_2O; (b) Magnification of area I; (c) Magnification of area II;
(d) H_2-H_2O; (e) Magnification of area III; (f) Magnification of area IV

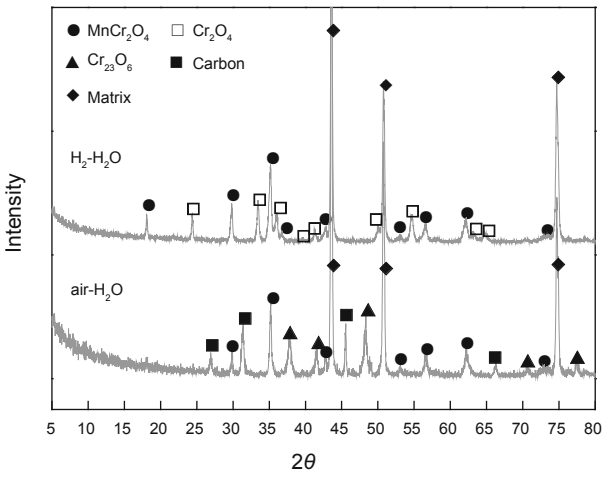

Fig. 7 XRD patterns of the inner surface oxidized in different atmospheres after 10 coking and decoking tests

the octahedral-shaped and standing blade $MnCr_2O_4$ spinels had high thermodynamic stability and good resistance to carburization (Li et al, 2009), and they remained unchanged after repeated coking and decoking tests. The dense standing blade $MnCr_2O_4$ spinels on the inner surface oxidized in H_2-H_2O isolated the hydrocarbon radicals from the elements Fe and Ni in the matrix alloy, so the formation of catalytic coke was inhibited effectively.

The pyrolysis gas, which contained H_2 and H_2O, also had a low oxygen partial pressure atmosphere, so it had the function of repairing the oxide films grown in H_2-H_2O and air-H_2O. However, there would be cracks and spallation in the oxide film inevitably after being used for a long time. The damaged areas contained a large amount of carbon and a small amount of Cr, Mn, such as point 1 in Fig. 6(b). It was very difficult for the dense $MnCr_2O_4$ spinels to be reproduced in these damaged areas, even if the oxide films were oxidized by H_2-H_2O or air-H_2O mixture again. The non-reproducibility could be the main weakness of the H_2-H_2O pre-oxidation technology.

3.4 Yield of pyrolysis products

The ethylene, propylene and butadiene yields in the naphtha pyrolysis tests in the two tubes covered with different oxide films are shown in Fig. 8. It was found that the yields of the main pyrolysis products in the tube oxidized in air-H_2O were almost the same as that in the tube oxidized in H_2-H_2O.

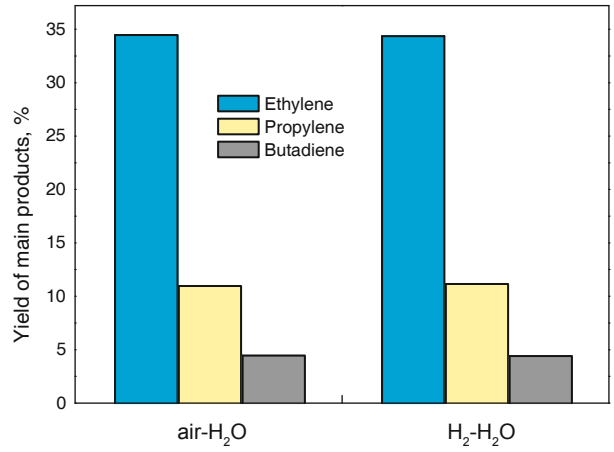

Fig. 8 Yields of main pyrolysis products in mini tubes oxidized in different atmospheres

4 Conclusions

The oxidation kinetics, surface morphology and phase structure of the oxide films grown on 25Cr20Ni alloy in air-H_2O and H_2-H_2O atmospheres at 900 ºC for 20 h were investigated in this paper. The anti-coking performance and resistance to carburization of the two oxide films were compared using mini tubes in a bench scale pyrolysis coking test. The results obtained are as follows:

1) The oxidation kinetics in the air-H_2O atmosphere followed a linear law in the initial stage and a parabolic law in the steady-state stage. The oxidation kinetics in H_2-H_2O atmosphere followed a linear law in the initial stage and a logarithm law in the steady-state stage.

2) The oxide film grown in the air-H_2O atmosphere had cracks, where the Fe and Ni were enriched and the un-cracked area was covered with octahedral-shaped $MnCr_2O_4$ spinels and $Cr_{1.3}Fe_{0.7}O_3$ oxide clusters, while the oxide film grown in the H_2-H_2O atmosphere was intact and completely covered with dense standing blade $MnCr_2O_4$ spinels.

3) In the bench scale pyrolysis coking test, the anti-coking performance of the tube oxidized in the H_2-H_2O atmosphere was far better than that oxidized in the air-H_2O atmosphere. The mass of coke in the tube oxidized in H_2-H_2O was only 8% of that in air-H_2O when the mass of coke stabilized after repeated coking and decoking tests.

4) The $Cr_{1.3}Fe_{0.7}O_3$ oxide clusters converted into $Cr_{23}C_6$ carbides, and carbon agglomerates were detected in the cracks after repeated coking and decoking tests on the oxide film grown in the air-H_2O atmosphere. However, the dense standing blade $MnCr_2O_4$ spinels remained unchanged in the oxide film grown in H_2-H_2O.

5) The ethylene, propylene and butadiene yields in the pyrolysis tests were almost the same for the two oxide films.

Acknowledgements

This research was financially supported by the scientific research project of China Petroleum and Chemical Corporation (No. 409075).

References

Albright L F and Marek J C. Mechanistic model for formation of coke in pyrolysis units producing ethylene. Industrial and Engineering Chemistry Research. 1988. 27(5): 755-759

Baker R T K, Gadsby G R, Thomas R B, et al. The production and properties of filamentous carbon. Carbon. 1975. 13(3): 211-214

Baker R T K. Catalytic growth of carbon filaments. Carbon. 1989. 27(3): 315-323

Benum L W and Oballa M C. Process of treating a stainless steel matrix. US Patent 6436202. 2002-08-20

Benum L W, Oballa M C and Petrone S S A. Surface on a stainless steel matrix. US Patent 6824883. 2004-11-30

Benum L W, Oballa M C and Petrone S S A. Surface on a stainless steel matrix. US Patent 7488392. 2009-02-10

Bonnet F, Ropital F, Berthier Y, et al. Filamentous carbon formation

caused by catalytic metal particles from iron oxide. Materials and Corrosion. 2003. 54(11): 870-880

Cai H Y, Krzywicki A and Oballa M C. Coke formation in steam crackers for ethylene production. Chemical Engineering and Processing. 2002. 41(3): 199-214

Deng W, Feng X J and Shi W Z. Studies of mechanism of coke formation during the pyrolysis of hydrocarbon. Shenyang Chemical Industry. 2000. 29(1): 23-26 (in Chinese)

Fisher G A, Prescott R, Chen Y, et al. Coating system for high temperature stainless steel. US Patent 6585864. 2003-06-01

Hammer J, Laney S, Jackson R, et al. The oxidation of ferritic stainless steels in simulated solid-oxide fuel-cell atmospheres. Oxidation of Metals. 2007. 67(1): 1-38

Hänsel M, Quadakkers W J and Young D J. Role of water vapor in chromia-scale growth at low oxygen partial pressure. Oxidation of Metals. 2003. 59(3-4): 285-301

Hua B, Lu F, Zhang J, et al. Oxidation behavior and electrical property of a Ni-based alloy in SOFC anode environment. Journal of the Electrochemical Society. 2009. 156(10): 1261-1266

Kofstad P. High Temperature Corrosion. London and New York: Elsevier Applied Science Press. 1988. 148

Li C S, Yu L and Yang Y S. Coking behavior of three kinds of metals and their oxide films during thermal pyrolysis reaction of hydrocarbons. Journal of Chinese Society for Corrosion and Protection. 2001. 21(3): 158-166 (in Chinese)

Li H, Zheng Y J, Benum L W, et al. Carburization behaviour of Mn-Cr-O spinel in high temperature hydrocarbon pyrolysis environment. Corrosion Science. 2009. 51(10): 2336-2341

Li T F. Metal High Temperature Oxidation and Hot Corrosion. Beijing: Chemical Industry Press. 2003. 53-61 (in Chinese)

Lobnig R E, Hennesen K, Grabke H J, et al. Diffusion of cations in chromia layers grown on iron-base alloys. Oxidation of Metals. 1992. 37(1-2): 81-93

Manafzadeh H, Sadrameli S M and Towfighi J. Coke deposition by physical condensation of poly-cyclic hydrocarbons in the transfer line exchanger (TLX) of olefin plant. Applied Thermal Engineering. 2003. 23(11): 1347-1358

Mott N F and Gurney R W. Electronic Process in Ionic Crystals. New York: Oxford University Press. 1940

Polman E A, Fransen T and Gellings P J. Oxidation kinetics of chromium and morphological phenomena. Oxidation of Metals. 1989. 32(5-6): 433-447

Povoden E, Grundy A N and Gauckler L J. Thermodynamic assessment of the Mn-Cr-O system for solid oxide fuel cell (SOFC) materials. International Journal of Materials Research. 2006. 97(5): 569-578

Raynaud G M and Rapp R A. In situ observation of whiskers, pyramids and pits during the high-temperature oxidation of metals. Oxidation of Metals. 1984. 21(1): 89-102

Susan D, Van Den Avyle J, Monroe S, et al. The effects of pre-oxidation and alloy chemistry of austenitic stainless steels on glass/metal sealing. Oxidation of Metals. 2009. 73(1): 311-335

Towfighi J, Sadrameli M and Niaei A. Coke formation mechanisms and coke inhibiting methods in pyrolysis furnaces. Journal of Chemical Engineering of Japan. 2002. 35(10): 923-937

Wynns K A and Bayer G T. Surface alloy system conversion for high temperature applications. US Patent 6537388. 2003-03-25

Zhou J X, Xu H, Luan X J, et al. Influence of the SiO_2/S coating and sulfur/phosphorus-containing coking inhibitor on coke formation during thermal pyrolysis of light naphtha. Fuel Processing Technology. 2012. 104: 198-203

Zurek J, Young D J, Essuman E, et al. Growth and adherence of chromia based surface scales on Ni-base alloys in high-and low-pO_2 gases. Materials Science and Engineering A. 2008. 477(1-2): 259-270

(Edited by Sun Yanhua)